Polyoxometalate as the assembly material to self-assembled Ni(OH)$_2$ nanosheets with electrocatalytic performance

Danyang He[1], Tianyang Li[1], Luozhen Jiang[2], Fei Wang[1], Zihao Xing[3], Nan Wang[1] (✉), Zhiyu Jia[1] (✉), and Guo-Yu Yang[1] (✉)

[1] *Key Laboratory of Cluster Science, Ministry of Education, School of Chemistry and Chemical Engineering, Beijing Institute of Technology, Beijing 100081, China*

[2] *Shanghai Advanced Research Institute, Chinese Academy of Science, Shanghai 201210, China*

[3] *Key Laboratory of Polyoxometalate and Reticular Material Chemistry of Ministry of Education, Facluty of Chemistry, Northeast Normal University, Changchun 130024, China*

ABSTRACT

Developing non-noble metal-based electrocatalyst with high catalytic activity is essential for advancing hydrogen energy technologies. This study introduces a hydrothermal method for synthesizing order Ni(OH)$_2$ nanosheets, with H$_3$O$_{40}$PW$_{12}$ (denoted as PW$_{12}$) loaded onto reduced graphene oxide (rGO) coated on nickel foam (referred to as PW$_{12}$-Ni(OH)$_2$/rGO). This method contrasts with the electrodeposition of Ni(OH)$_2$, where PW$_{12}$ is added to the synthetic system to direct the assembly and morphology of the Ni(OH)$_2$ through a hydrothermal reaction. In this work, the nickel foam acts dual roles as both the substrate and the source of nickel for the formation of Ni(OH)$_2$. The PW$_{12}$-Ni(OH)$_2$/rGO nanosheets, when successfully prepared and loaded onto the nickel foam (NF), exhibited superior electrocatalytic activity for the hydrogen evolution reaction (HER) in an alkaline electrolyte, achieving a current density of 10 mA·cm^{-2} at an overpotential of 69 mV. Furthermore, we endeavored to expand the application of this material towards the oxygen evolution reaction (OER) by preparing PW$_{12}$-(Fe/Co)Ni(OH)$_2$/rGO through the addition of metal cations. This nanocomposite displayed outstanding electrocatalytic activity in alkaline electrolytes, with a current density of 10 mA·cm^{-2} at an overpotential of 211 mV, and demonstrated excellent stability over a 50 h period in a 1 M KOH solution. The results presented in this paper offer an effective strategy for the preparation of polyoxometalate-based inorganic materials with diverse functionalities, applicable to both HER and OER.

KEYWORDS

polyoxometalate, Ni(OH)$_2$, assembly, hydrogen evolution reaction, oxygen evolution reaction

1 Introduction

Hydrogen energy, as a potential clean energy source, has been developed to replace fossil fuels in various fields, addressingthe global energy shortage [1, 2]. With the growing demand for hydrogen energy, there is a need for electrocatalysts capable of withstanding large currents for water electrolysis. Noble-metal-based electrocatalysts, such as platinum (Pt) and iridium (Ir), have shown high electrocataltyic activity towards both hydrogen evolution reaction (HER) and oxygen evolution reaction (OER) [3–9]. However, the high cost and limited availability of of these noble metals restrict their widespread industrial application. Consequently, numerous researchers are focusing on the design and synthesis of non-noble metal-based electrocatalysts with remarkable catalytic acitivity for HER and OER [10–14].

Polyoxometalates (POMs) constitute one of the largest families of nanocluster metal oxides, composed of cationic and polyanionic clusters, which endow them with remarkabel redox properties. As the building blocks for assemblies, POMs offer high electronic diversity and exhibit superior catalytic performance in redox reactions [15–17]. Over the past two decades, polyoxometalate-based inorganic materials, in their nanoscale form, have been extensively explored for their use in organic reaction, electrochemical reactions, and energy [18–23]. To deversify the physicochemical properties and applications of POMs, inorganic hybrid materials have been designed and prepared. For example, the encapuslation of POMs within metal-organic frameworks (MOF) is an effective strategy for catalytic oxidation reactions [24]. The Dexter-Silverton structure POM, when loaded onto fluoro-graphdiyne, has been shown to provide superior performance and stability for OER [25]. Additionally, helical microporous nanorods (HMNRs) have been synthesized through the assembly of POM clusters and cationic surfactants, combining the redox catalytic properties of POMs with the unique structural attributes of microporous materials [26].

In this work, we have reported a hydrothermal method for the synthesis of ordered Ni(OH)$_2$ nanosheets (NSs) with H$_3$O$_{40}$PW$_{12}$ (PW$_{12}$) loaded on reduced graphene oxide (rGO)-coated Ni foam, denoted as PW$_{12}$-Ni(OH)$_2$/rGO. Compared with the electrodeposition method for preparing Ni(OH)$_2$, the polyoxometalate cluster serves as a director for the assembly and morphology of Ni(OH)$_2$. The Ni foam functions not only as the substrate but also as the source of Ni for the formation of Ni(OH)$_2$, eliminating the need for additional Ni^{2+}. The PW$_{12}$-

$Ni(OH)_2$/rGO nanosheets exhibited superior electrocatalytic activity for HER in alkaline electrolyte. To further optimize the catalytic activity for OER, we assembled the electrode PW_{12}-$Ni/Co/Fe(OH)_2$/rGO nanosheets through the additional of Co^{2+} and Fe^{2+}. This composite demonstrated superior electrocatalytic activity towards OER. Based on the above research, we have identified that PW_{12} is a superior assembly for POM-based inorganic materials.

2 Experimental

2.1 Fabrication of rGO@Ni foam

Mercantile nickel foam (NF) with dimensions of 1 cm × 2 cm was washed sequentially with an aqueous HCl solution (1 M), deionized water and ethanol solution, respectively. Graphene oxide (GO, 20 mg) was ultrasonically treated for 1 h in 20 mL deionized water. Then, an additional 10 mL of water was added, and the mixture was transferred to a 50 mL Teflon-lined stainless steel autoclave, along with the pre-processed NF. The NF was then completely soaked in the hydrothermal reaction solution at 160 °C for 24 h. Afterward, the autoclave was allowed to cool to room temperature, the NF was washed with deionized water and ethanol, and subsequently dried under vacuum at 60 °C overnight.

2.2 Fabrication of PW_{12}-$Ni(OH)_2$/rGO

NH_4F (2 mmol), urea (5 mmol), and $H_3O_{40}PW_{12}$ (0.5 mmol) were mixed into 28 mL of deionized water and 5 mL of ethanol, stirred for 1 h, and then transferred into 50 mL Teflon-lined stainless steel autoclave. Subsequently, a piece of dry rGO@NF was added, and the mixture was subjected to a hydrothermal reaction at 120 °C for 5 h. Afterward, the autoclave was allowed to cool to room temperature. The NF was then washed with deionized water and ethanol, and dried under vacuum at 60 °C overnight.

2.3 Fabrication of PW_{12}-$(Fe/Co)Ni(OH)_2$/rGO

$FeCl_2$ (0.25 mmol), $Co(NO_3)_2 \cdot 6H_2O$ (1 mmol), NH_4F (2 mmol), urea (5 mmol), and $H_3O_{40}PW_{12}$ (0.5 mmol) were mixed into 28 mL of deionized water and 5 mL of ethanol, stirred for 1 h, and then transferred into 50 mL Teflon-lined stainless steel autoclave.

A piece of dry rGO@NF was added, and the mixture was subjected to a hydrothermal reaction at 120 °C for 5 h. Afterward, the autoclave was allowed to cool to room temperature. The NF was then washed with deionized water and ethanol and dried under vacuum at 60 °C overnight.

3 Results and discussion

According to the traditional method for preparing $Ni(OH)_2$-based electrode, $NiCl_2 \cdot 6H_2O$ is required as the Ni source [27–29]. Controlling the concentration of Ni^{2+} is a critical factor in preparing $Ni(OH)_2$-based electrodes. The POM-hybrid is an effective approach to enhance electrocatalytic activity. Different concentrations of PW_{12} affect the pH of the system, and the dissolution of NF varies in different pH environments [30–34]. Based on the aforementioned experiments, we have developed a novel method for preparing the POM-hybrid $Ni(OH)_2$-based electrode. The synthesis process of PW_{12}-$Ni(OH)_2$/rGO electrode is depicted in Fig. 1(a). To increase the electroconductivity and the specific area of the Ni foam, graphene oxide was reduced on the surface of the Ni foam (rGO@Ni foam) in the first step. Subsequently, in the second step, PW_{12} not only acts as acid catalysts for the dissolution of Ni foam into a Ni source but also serves as a co-catalyst hybridized with $Ni(OH)_2$ through a hydrothermal method. The acidity of PW_{12} is a key factor in dissolving Ni foam, enabling the growth of $Ni(OH)_2$ nanosheets from the three-dimensional (3D) porous structure of rGO. We tested various concentrations of PW_{12}: 0.1, 0.3, 0.5, 0.6, 0.7, and 0.9 mmol, respectively. From Figs. 1(b)−1(g), we determined that a PW_{12} concentration of 0.5 mmol was optimal for preparing uniform $Ni(OH)_2$ nanosheets, which could compete favorably with the traditional method using a Ni source. The scanning electron microscopy (SEM) images revealed that PW_{12} exhibits superior acidity for dissolving Ni foam, surpassing that of inorganic acids such as HCl (Fig. S12(a) in the Electronic Supplementary Material (ESM)). In summary, we have identified a new method for preparing $Ni(OH)_2$ nanosheets with POM, which could prove to be a valuable POM-based inorganic material.
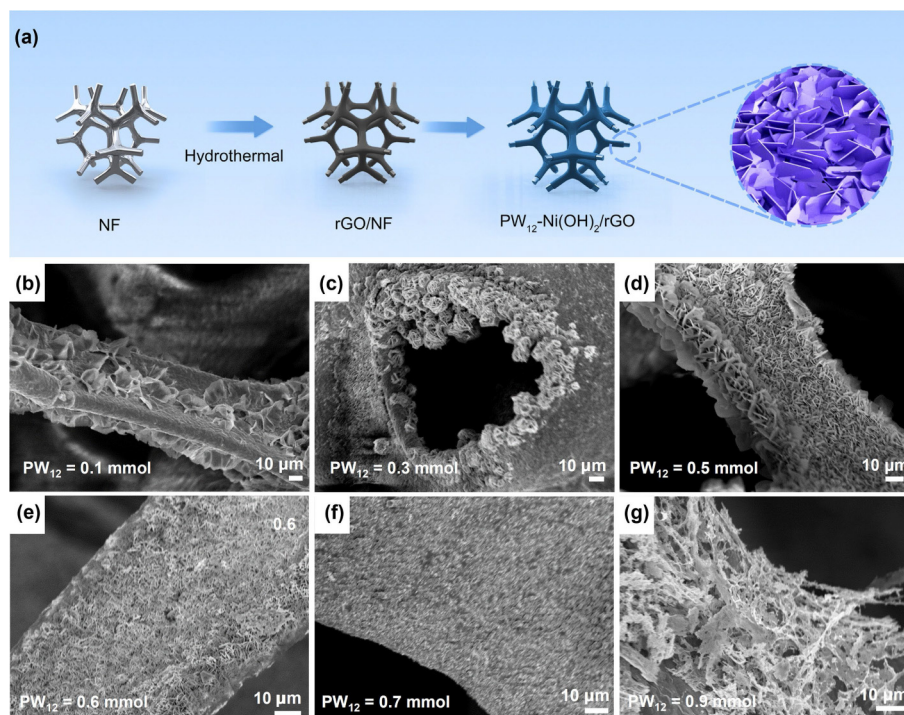
To identify the structure and chemical composition of the

Figure 1 (a) Illustration of the preparation of the PW_{12}-$Ni(OH)_2$/rGO electrode. (b)–(g) The morphology of PW_{12}-$Ni(OH)_2$/rGO with the different concentration of PW_{12} (0.1, 0.3, 0.5, 0.6, 0.7, and 0.9 mmol).

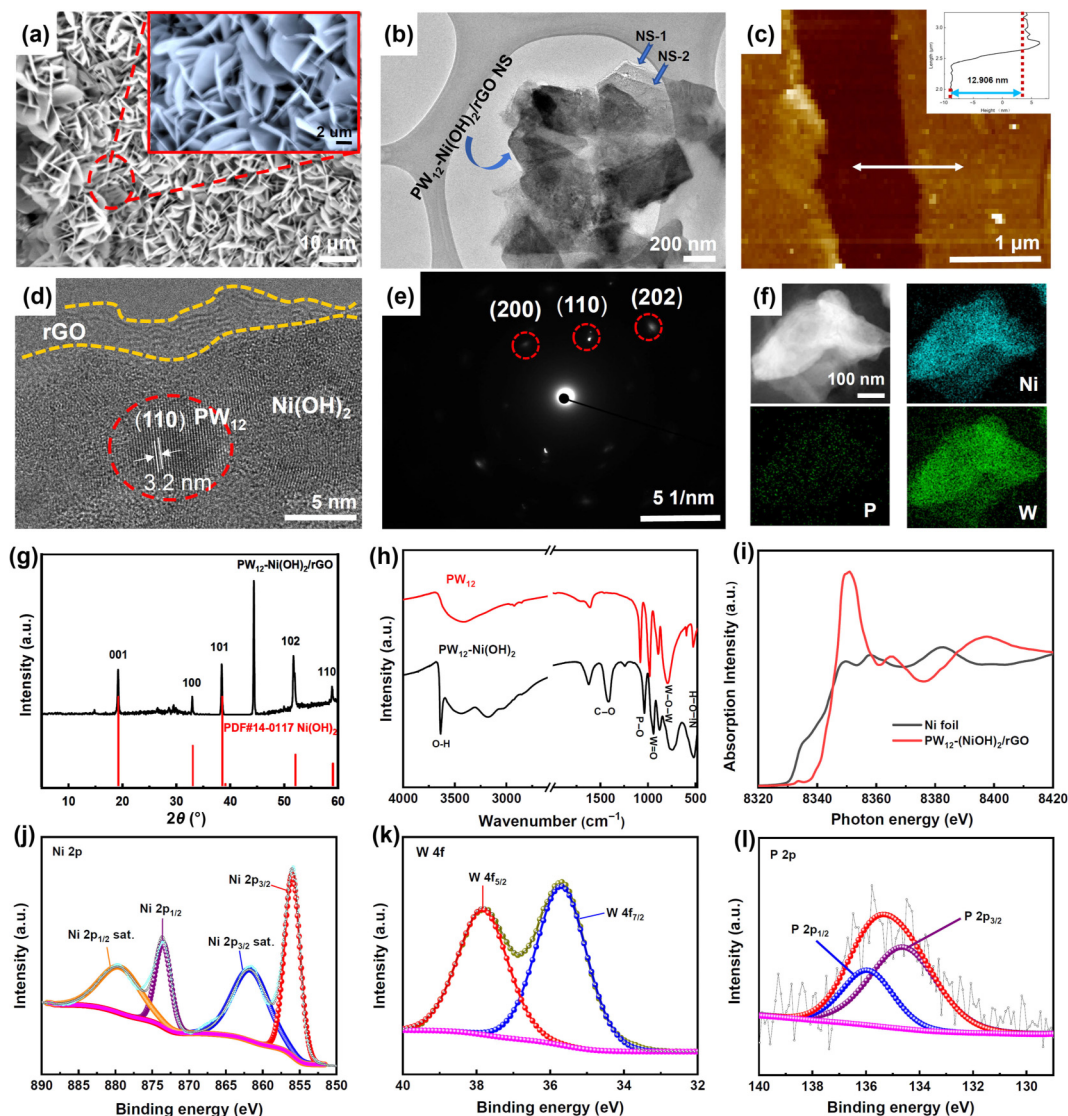**Figure 2** (a) SEM images about the morphology of PW_{12}-$Ni(OH)_2$/rGO nanosheets on Ni foam. (b) TEM image of PW_{12}-$Ni(OH)_2$/rGO nanosheets. (c) The thickness of PW_{12}-$Ni(OH)_2$/rGO nanosheets tested by AFM. (d) Magnified HRTEM image of PW_{12}-$Ni(OH)_2$/rGO nanosheets, and (e) the corresponding fast Fourier transforms. (f) Scanning TEM image of PW_{12}-$Ni(OH)_2$/rGO nanosheet and the corresponding element mapping of Ni, P, W. (g) PXRD data of PW_{12}-$Ni(OH)_2$/rGO. (h) IR spectra of PW_{12}-$Ni(OH)_2$/rGO and PW_{12}. (i) Ni K-edge XANES spectra of PW_{12}-$Ni(OH)_2$/rGO and Ni foil. High-resolution XPS spectrum of PW_{12}-$Ni(OH)_2$/rGO showing (j) Ni 2p, (k) W 4f, and (l) P 2p.

aforementioned material, SEM architecture could provide more catalytic centers. From the transmission electron microscopy (TEM) image in Fig. 2(b), the nanosheet structure was further confirmed. For instance, the overlapping structure between nanosheet-1 (NS-1) and nanosheet-2 (NS-2) can be clearly observed, which is similar to that observed with SEM. Moreover, the thickness of the NS is a typical parameter for evaluating the hybrid capability of PW_{12}. In Fig. 2(c), an atomic force microscope (AFM) was used to measure the thickness of the NS, which was found to be 12.906 nm—sufficient to provide space for POM hybridization. Additionally, the high-resolution TEM (HRTEM) image in Fig. 2(d) shows that PW_{12} (110) has successfully hybridized with the $Ni(OH)_2$ nanosheets [35]; rGO is also observed, which can be attributed to the edges of the NS on the Ni foam. The corresponding selected-area electron diffraction (SAED) patterns reveal lattice fringes whose spacings are consistent with the (200), (110), and (202) planes of the $Ni(OH)_2$ lattice (Fig. 2(e)), thus supporting the structural assignment [36]. Furthermore, the scanning TEM and corresponding elemental mapping results (Fig. 2(f)) demonstrate the homogeneous distribution of Ni, P, and W across the entire nanosheet.

Due to the synthesis method being different from the traditional method, we should use additional characterizations to

confirm that the nanosheets are indeed $Ni(OH)_2$. Firstly, the powder X-ray diffraction (PXRD) of PW_{12}-$Ni(OH)_2$/rGO indicates that the crystal lattice corresponds to $Ni(OH)_2$ [24]. Then, infrared (IR) spectroscopy was further used to identify the structure of PW_{12}-$Ni(OH)_2$/rGO_2, the peaks at 535 and 3635 cm^{-1} could be attributed to Ni–O–H and O–H, respectively. There are three distinct peaks at 1035 cm^{-1} for P–O, 944 cm^{-1} for Mo=O, 869 cm^{-1} for Mo–O–Mo, which can be attributed to PW_{12}. The peak at 1421 cm^{-1} can be attributed to the C–O of rGO. Based on the IR data, we can confirm that PW_{12} had hybridized on $Ni(OH)_2$, indicating that the POM-based inorganic material (PW_{12}-$Ni(OH)_2$/rGO) has been successfully prepared. We then proceeded to ascertain the structure of PW_{12}-$Ni(OH)_2$/rGO using extended X-ray absorption fine structure (EXAFS). The energy absorption at the Ni K-edge X-ray absorption near edge structure (XANES, as shown in Fig. 2(i)) confirms that the structure is indeed $Ni(OH)_2$ [37]. Concurrently, X-ray photoelectron spectroscopy (XPS) was performed to analyze PW_{12}-$Ni(OH)_2$/rGO. Figure 2(j) showed the high-resolution spectrum of Ni 2p, with the main Ni $2p_{3/2}$ peak and its satellite peaks at 855.9 and 861.8 eV, and the Ni $2p_{1/2}$ main peak and its satellite peaks at 873.6 and 880.1 eV, respectively. Two signals for W^{6+} ($4f_{7/2}$ and $4f_{5/2}$) are observed at 35.9 and 38.1 eV (Fig. 2(k)) [38].

Furthermore, the P 2p high-resolution spectrum (Fig. 2(l)) can be resolved into P–O [39]. The XPS data further confirms that PW_{12} had been hybridized on $Ni(OH)_2$.

According to the above data, the new method for preparing the POM-based inorganic materials PW_{12}-$Ni(OH)_2$/rGO through the assembly of the PW_{12} cluster and $Ni(OH)_2$ has been established successfully.

Then, we applied PW_{12}-$Ni(OH)_2$/rGO as the electrocatalyst for the HER. Its electrocatalytic performance toward water oxidation was investigated in a 1.0 M KOH solution at room temperature using a standard three-electrode system setup. This setup included a working electrode PW_{12}-$Ni(OH)_2$/rGO, a standard calomel reference electrode (SCE), and a graphite rod counter electrode. The original PW_{12}-$Ni(OH)_2$/rGO, HCl-$Ni(OH)_2$/rGO, PMo_{12}-$Ni(OH)_2$/rGO, SiW_{12}-$Ni(OH)_2$/rGO and SiW_{11}-$Ni(OH)_2$/rGO were tested as references under the same conditions. The linear sweep voltammetry (LSV) curves of all samples were tested at a scan rate of 5 mV·s^{-1}. As shown in Fig. 3(a), PW_{12}-$Ni(OH)_2$/rGO exhibited an earlier onset potential of 236 mV (vs. RHE) and a higher current density than HCl-$Ni(OH)_2$/rGO, PMo_{12}-$Ni(OH)_2$/rGO, SiW_{12}-$Ni(OH)_2$/rGO and SiW_{11}-$Ni(OH)_2$/rGO, suggesting its improved and remarkable activity. It requires a potential of 236 mV (vs. RHE) to reach 50 mA·cm^{-2}, which is lower than that of HCl-$Ni(OH)_2$/rGO (292 mV vs. RHE), PMo_{12}-$Ni(OH)_2$/rGO (338 mV vs. RHE), SiW_{12}-$Ni(OH)_2$/rGO (372 mV vs. RHE) and SiW_{11}-$Ni(OH)_2$/rGO (426 mV vs. RHE). In addition, the catalytic activity could be achieved with a low potential of 700 mV (vs. RHE) at a high current density (358 mA·cm^{-2}). Moreover, as shown in Fig. 3(b), the Tafel slopes of PW_{12}-$Ni(OH)_2$/rGO, HCl-$Ni(OH)_2$/rGO, PMo_{12}-$Ni(OH)_2$/rGO, SiW_{12}-$Ni(OH)_2$/rGO and SiW_{11}-$Ni(OH)_2$/rGO are 129, 407, 281, 367 and 255 mV·dec^{-1}, respectively, confirming the superior catalytic kinetics of PW_{12}-$Ni(OH)_2$/rGO.

Operating under basic aqueous conditions, corrosion resistance is the most important parameter affecting the performance of the OER, including both its activity and stability. Remarkably, in this work, rGO could not only effectively protected the activity center

but also increased the electroconductivity. To evaluate the long-term stability of the electrode, we conducted chronoamperometry measurements with a −0.334 V (vs. RHE) bias at a pH of 14, the PW_{12}-$Ni(OH)_2$/rGO electrode displayed a current density of 100 mA·cm^{-2}, which decreased to 4 mA·cm^{-2} after 50 h (Fig. 3(c)). However, at the same applied potentials, the HCl-$Ni(OH)_2$/rGO, PMo_{12}-$Ni(OH)_2$/rGO, SiW_{12}-$Ni(OH)_2$/rGO and SiW_{11}-$Ni(OH)_2$/rGO electrodes exhibited a much worse stability (Fig. S29 in the ESM). This suggests that the encapsulation of rGO in $Ni(OH)_2$ is an effective way to enhance the stability of the electrode. Furthermore, the stability of PW_{12}-$Ni(OH)_2$/rGO was also assessed with post catalytic SEM and LSV analysis. The morphology can be clearly observed, being the same as that of the original electrode in Fig. S29 in the ESM. The above experimental data also indicate that the PW_{12}-$Ni(OH)_2$/rGO electrode maintains high catalytic performance after 50 h chronoamperometry measurements for the OER in alkaline electrolytes.

The electrochemically active surface area (ECSA) of all samples was evaluated by measuring the electrochemical double-layer capacitances (C_{dl}) in 1 M KOH via cyclic voltammetry at different scan rates (Fig. S28 in the ESM). The C_{dl} of PW_{12}-$Ni(OH)_2$/rGO is 9.78 mF·cm^{-2} (Fig. 3(d)), higher than that of HCl-$Ni(OH)_2$/rGO (4.03 mF·cm^{-2}), PMo_{12}-$Ni(OH)_2$/rGO (5.27 mF·cm^{-2}), and SiW_{12}-$Ni(OH)_2$/rGO (1.93 mF·cm^{-2}). Next, we investigated the catalytic kinetics of the reactions at the electrode/electrolyte interface by electrochemical impedance spectroscopy (EIS). As shown in Fig. S30(a) in the ESM, PW_{12}-$Ni(OH)_2$/rGO has the lowest solution resistance (R_s = 1.28 Ω) and charge-transfer resistance (R_{ct} = 4.72 Ω), indicating faster charge-transfer behavior. This demonstrates that PW_{12} provides a faster electron and mass transfer pathway, leading to an improvement in the catalytic performance. The recorded impedance data were fitted using a circuit model (Fig. S30(b) in the ESM).

Up to this point, PW_{12}-based inorganic material has exhibited the catalytic activity towards HER. For expanding its application for OER, we attempted to prepare a series of new PW_{12}-$Ni(OH)_2$/rGO by adding of metal cationic (Co^{2+}/Fe^{2+}, Co^{2+} and Fe^{2+},
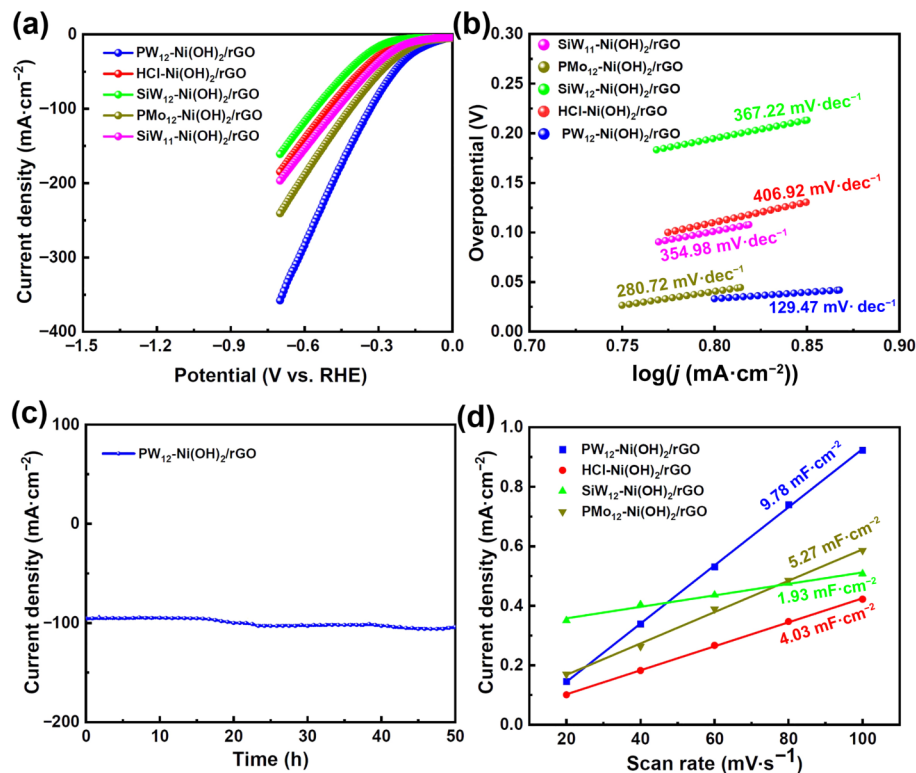
Figure 3 (a) LSV polarization curves of PW_{12}-$Ni(OH)_2$/rGO, HCl-$Ni(OH)_2$/rGO, PMo_{12}-$Ni(OH)_2$/rGO, SiW_{12}-$Ni(OH)_2$/rGO and SiW_{11}-$Ni(OH)_2$/rGO in 1 M KOH. (b) Tafel plots of PW_{12}-$Ni(OH)_2$/rGO, HCl-$Ni(OH)_2$/rGO, PMo_{12}-$Ni(OH)_2$/rGO, SiW_{12}-$Ni(OH)_2$/rGO and SiW_{11}-$Ni(OH)_2$/rGO in 1 M KOH. (c) Stability test results of PW_{12}-$Ni(OH)_2$/rGO at 1.56 V (vs. RHE). (d) Plots of the current density differences vs. the scan rate for various catalysts.

respectively) with more catalytic center, resulting in the corresponding electrodes PW_{12}-(Fe/Co)Ni(OH)$_2$/rGO, PW_{12}-(Fe)Ni(OH)$_2$/rGO and PW_{12}-(Co)Ni(OH)$_2$/rGO.

SEM and TEM images of PW_{12}-(Fe/Co)Ni(OH)$_2$/rGO revealed a hierarchical nanostructure of microscale plate, which can facilitate ion contact with electrolyte and the expose of active sites. As shown in Fig. 4(a), the PW_{12}-(Fe/Co)Ni(OH)$_2$/rGO nanosheet deposit homogeneously and densely on the surface of NF. From TEM image of PW_{12}-(Fe/Co)Ni(OH)$_2$/rGO in Fig. 4(b), we could obverse the morphology of nanosheet, which is similar to that in the SEM image in Fig. 2(a). Additional, the IR spectrum (Fig. 4(c)) was the typical characterization for confirming the structure of PW_{12}-(Fe/Co)Ni(OH)$_2$/rGO was not only similar with the structure of PW_{12}-Ni(OH)$_2$/rGO, but also composed of PW_{12} and Ni(OH)$_2$.

For better characterization of PW_{12}-(Fe/Co)Ni(OH)$_2$/rGO, pure PW_{12}-(Fe/Co)Ni(OH)$_2$/rGO, which was removed from the NF by sonication, was analyzed by XPS. The XPS spectra of PW_{12}-(Fe/Co)Ni(OH)$_2$/rGO exhibit Fe 2p, Co 2p, and Ni 2p compositions from Figs. 4(d)–4(f). The Fe 2p region (Fig. 4(d)) comprises four easily discernible features: the Fe $2p_{3/2}$ spectrum generally show a main peak at 711.78 eV, accompanied by a shake-up satellite at 716.04 eV, indicating the presence of Fe^{3+} cations. The Co 2p region (Fig. 4(e)) also comprises four easily discernible features: the main Co $2p_{3/2}$ peak and its satellite peaks at 780.93 and 784.08 eV, respectively, and the Co $2p_{1/2}$ main peak and its

satellite peaks at 796.72 and 803.61 eV, respectively. It can be judged that Co is mainly Co–OH, with the oxidation state of Co being Co(II). In addition, there are four peaks for the Ni 2p signal in the binding energy range of 855–884 eV (Fig. 4(f)), The energy difference between the Ni $2p_{3/2}$ and Ni $2p_{1/2}$ in the fine Ni 2p spectrum is about 17.3 eV, and the spectral peak area ratio (Ni $2p_{3/2}$:Ni $2p_{1/2}$) is about 2:1. According to the energy position of the Ni $2p_{3/2}$ peak (about 856.1 eV) and the satellite peaks (about 861.6 eV), it can be judged that Ni is mainly present as NiOOH, with the oxidation state of Ni being Ni(II). Overall, the XPS data of PW_{12}-(Fe/Co)Ni(OH)$_2$/rGO further verify its structure [30].

The PW_{12}-(Fe/Co)Ni(OH)$_2$/rGO with its well-defined structure and chemical compositions, is applied as the electrocatalyst for OER in 1.0 M KOH. To identify the effect of PW_{12}-(Fe/Co)Ni(OH)$_2$/rGO, PW_{12}-(Fe)Ni(OH)$_2$/rGO and PW_{12}-(Co)Ni(OH)$_2$/rGO as reference electrodes were tested under the same conditions. The linear scanning voltammetry (LSV) curves of all the electrodes were measured at a scan rate of 5 mV·s⁻¹. As exhibited in Fig. 5(a), PW_{12}-(Fe/Co)Ni(OH)$_2$/rGO had the highest electrocatalytic activity, offering an overpotential of 211 mV at a current density of 10 mA·cm⁻², which is smaller than that of PW_{12}-(Fe)Ni(OH)$_2$/rGO (341 mV), PW_{12}-(Co)Ni(OH)$_2$/rGO (255 mV). In addition, the Tafel slope is also an important factor for evaluating OER kinetics. As displayed in Fig. 5(b), the Tafel slopes of PW_{12}-(Fe/Co)Ni(OH)$_2$/rGO, PW_{12}-(Fe)Ni(OH)$_2$/rGO, and PW_{12}-(Co)Ni(OH)$_2$/rGO are 66.53, 129.18, and 168.62 mV·dec⁻¹,
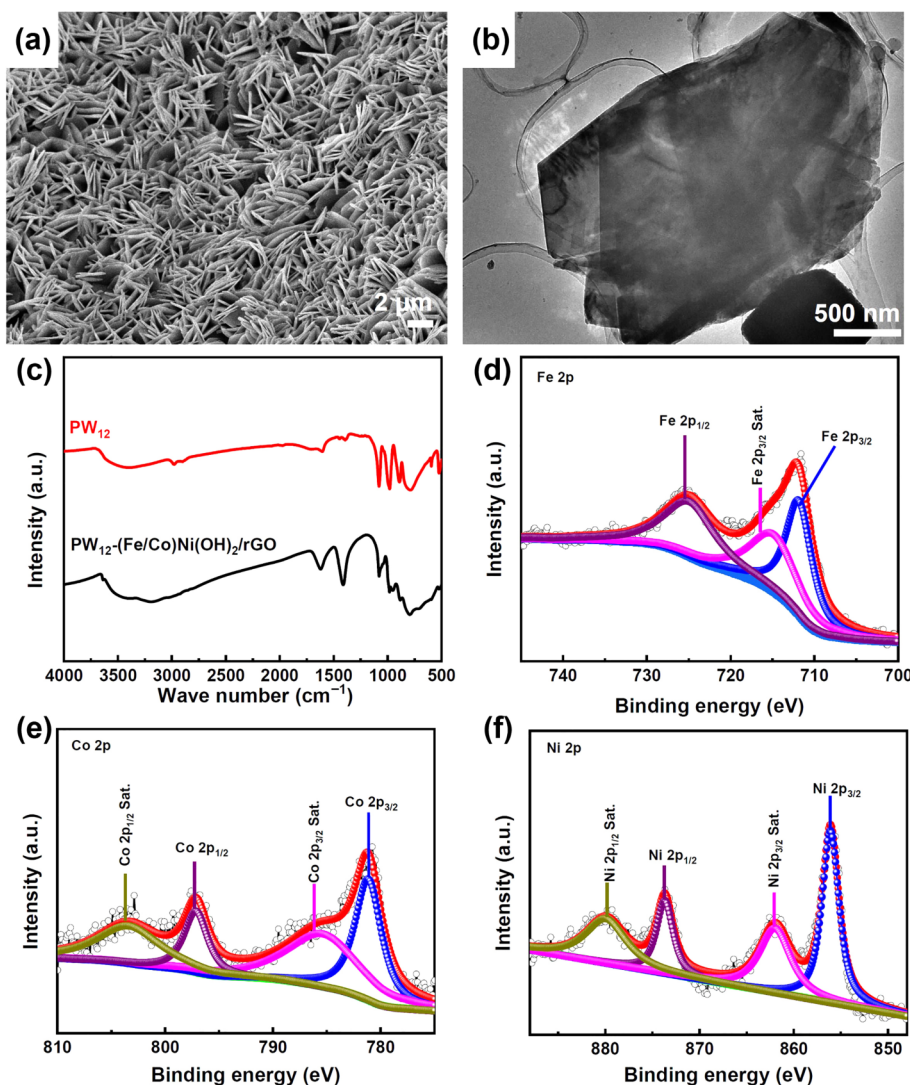

Figure 4 (a) SEM image about the morphology of PW_{12}-(Fe/Co)Ni(OH)$_2$/rGO nanosheets on Ni foam. (b) TEM image of PW_{12}-(Fe/Co)Ni(OH)$_2$/rGO nanosheets. (c) IR spectra of PW_{12}-(Fe/Co)Ni(OH)$_2$/rGO and PW_{12}. High-resolution XPS spectrum of PW_{12}-(Fe/Co)Ni(OH)$_2$/rGO showing (d) Fe 2p; (e) Co 2p, and (f) Ni 2p.

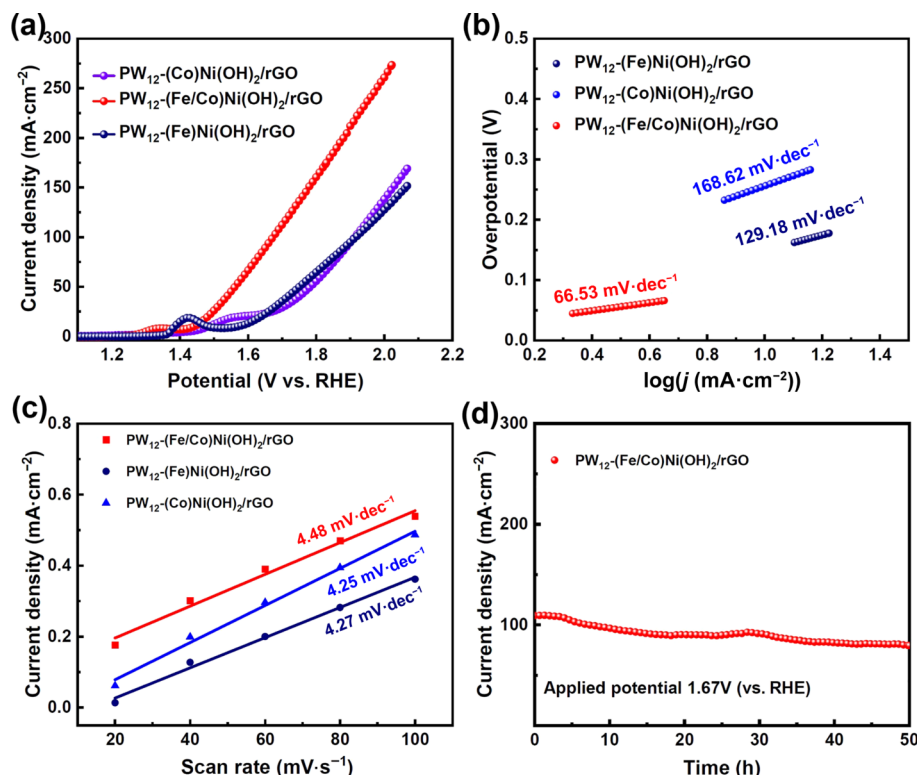**Figure 5** (a) LSV polarization curves of PW_{12}-(Fe/Co)Ni(OH)$_2$/rGO, PW_{12}-(Fe)Ni(OH)$_2$/rGO and PW_{12}-(Co)Ni(OH)$_2$/rGO in 1 M KOH. (b) Tafel slope of PW_{12}-(Fe/Co)Ni(OH)$_2$/rGO, PW_{12}-(Fe)Ni(OH)$_2$/rGO and PW_{12}-(Co) Ni(OH)$_2$/rGO. (c) Plots of the current density differences vs. the scan rate for various catalysts. (d) Stability test results of PW_{12}-(Fe/Co)Ni(OH)$_2$/rGO at 1.67 V (vs. RHE).

respectively, which supports PW_{12}-(Fe)Ni(OH)$_2$/rGO (341 mV) has excellent catalytic kinetics.

The electrochemical activity surface area (ECSA) was utilized to investigate the superior OER performance of PW_{12}-(Fe/Co) Ni(OH)$_2$/rGO. Initially, the C_{dl} is determined by cyclic voltammetry at varying scan rates (Fig. S27 in the ESM). The C_{dl} of PW_{12}-(Fe/Co)Ni(OH)$_2$/rGO is measured at 4.48 mF·cm^{-2}, which is higher than that of PW_{12}-(Fe)Ni(OH)$_2$/rGO at 4.27 mF·cm^{-2} and PW_{12}-(Co)Ni(OH)$_2$/rGO at 4.25 mF·cm^{-2}. Furthermore, the stability of PW_{12}-(Fe /Co)Ni(OH)$_2$/rGO is demonstrated in Fig. 5(c). Using chronoamperometry measurements with a bias of 1.67 V (vs. RHE) bias at a pH of 14, the PW_{12}-(Fe/Co)Ni(OH)$_2$/rGO electrode exhibited a current density of 100 mA·cm^{-2}, which gradually decreased to 20 mA·cm^{-2} after 50 h (Fig. 5(d)). In addition to chronoamperometry measurements, SEM and LSV analysis were conducted on the PW_{12}-(Fe/Co)Ni(OH)$_2$/rGO electrode. The regularly nanosheets are observed to lie on the NF, indicating that the structure of PW_{12}-(Fe/Co)Ni(OH)$_2$/rGO is structurally intact. In conclusion, PW_{12}-(Fe/Co)Ni(OH)$_2$/rGO exhibits remarkable OER performance, where metal ions play a regulating role in the construction of composite materials.

4 Conclusions

Based on our previous research of electrocatalysts composed of polyoxometalate and non-noble metal, we have developed a method to prepare POM hybrid Ni(OH)$_2$ nanosheets on rGO. The nanosheet structure provides a large surface area for catalytic reactions, and the rGO offers excellent electrical conductivity. During the synthesis process, PW_{12} exhibited two key mechanisms for the electrode with electrochemical performance: (i) The acitity of PW_{12}, a vital factor for dissolving Ni foam, which provides the Ni source for the preparation of Ni(OH)$_2$ nanosheets; (ii) PW_{12} acts as a co-catalysts of Ni(OH)$_2$, enhancing the electrocatalytic activity for HER in alkaline conditions, which is superior to other POMs. PW_{12} is not only the superior assembly agent but also a

catalytic center for the PW_{12}-Ni(OH)$_2$/rGO electrode. The interaction between the Ni(OH)$_2$ and the POM could lead to enhanced catalytic activity due to the synergy between Ni(OH)$_2$ and POM. Our findings offer new insights for the development of POM-based inorganic materials.

References

[1] Chu, S.; Majumdar, A. Opportunities and challenges for a sustainable energy future. *Nature* **2012**, *488*, 294–303.

[2] Jiao, Y.; Zheng, Y.; Jaroniec, M.; Qiao, S. Z. Design of electrocatalysts for oxygen- and hydrogen-involving energy conversion reactions. *Chem. Soc. Rev.* **2015**, *44*, 2060–2086.

[3] Wang, Y. D.; Wu, W.; Chen, R. Z.; Lin, C. X.; Mu, S. C.; Cheng, N. C. Reduced water dissociation barrier on constructing Pt-Co/CoO$_x$ interface for alkaline hydrogen evolution. *Nano Res.* **2022**, *15*, 4958–4964.

[4] Qi, J.; Zhong, X. Y.; Zeng, H. Y.; Wang, C.; Liu, Z. F.; Chen, J. J.; Gu, L.; Hong, E. N.; Li, M. X.; Li, J. et al. *In-situ* study for the elastic structure evolutions of three-dimensional Ir–O framework during the oxygen evolution reaction in acid. *Nano Res.* **2023**, *16*, 9022–9030

[5] Qin, J. S.; Xie, T. H.; Zhou, D. J.; Luo, L.; Zhang, Z. Y.; Shang, Z.

C.; Li, J. W.; Mohapatra, L.; Yu, J. W.; Xu, H. J. et al. Kinetic study of electrochemically produced hydrogen bubbles on Pt electrodes with tailored geometries. *Nano Res.* **2021**, *14*, 2154–2159.

[6] Song, Z. P.; Yi, J. Z.; Qi, J.; Zheng, Q.; Zhu, Z. L.; Tao, L.; Cao, Y.; Li, Y.; Gao, Z. Y.; Zhang, R. Z. et al. Line defects in monolayer TiSe₂ with adsorption of Pt atoms potentially enable excellent catalytic activity. *Nano Res.* **2022**, *15*, 4687–4692.

[7] Mu, X. Q.; Zhang, X. Y.; Chen, Z. Y.; Gao, Y.; Yu, M.; Chen, D.; Pan, H. Z.; Liu, S. L.; Wang, D. S.; Mu, S. C. Constructing symmetry-mismatched $Ru_xFe_{3-x}O_4$ heterointerface-supported Ru clusters for efficient hydrogen evolution and oxidation reactions. *Nano Lett.* **2024**, *24*, 1015–1023.

[8] Mu, X. Q.; Gu, X. Y.; Dai, S. P.; Chen, J. B.; Cui, Y. J.; Chen, Q.; Yu, M.; Chen, C. Y.; Liu, S. L.; Mu, S. C. Breaking the symmetry of single-atom catalysts enables an extremely low energy barrier and high stability for large-current-density water splitting. *Energy Environ. Sci.* **2022**, *15*, 4048–4057.

[9] Zheng, X. B.; Yang, J. R.; Li, P.; Wang, Q. S.; Wu, J. B.; Zhang, E. H.; Chen, S. H.; Zhuang, Z. C.; Lai, W. H.; Dou, S. X. et al. Ir-Sn pair-site triggers key oxygen radical intermediate for efficient acidic water oxidation. *Sci. Adv.* **2023**, *9*, eadi8025.

[10] Ping, J. J.; He, D. Y.; Wang, F.; Wang, N.; Fu, Y. C.; Xing, Z. H.; Jia, Z. Y.; Yang, G. Y. Nanocomposite: Keggin-type Co₄-polyoxometalate@cobaltporphyrin linked graphdiyne for hydrogen evolution in seawater. *Nano Res.* **2023**, *17*, 1281–1287.

[11] Xu, X. M.; Wang, Y. C.; Shang, W. H.; Wang, F.; Zhang, Q.; Li, K.; Wu, M.; Jia, Z. Y. Cobalt carbonate hydroxides anchored on nanoscale pyrenely-graphdiyne nanowalls toward bifunctional electrocatalysts with high performance and stability for overall water splitting. *New J. Chem.* **2023**, *47*, 11594–11601.

[12] Hu, Y. M.; Chao, T. T.; Li, Y. P.; Liu, P. G.; Zhao, T. H.; Yu, G.; Chen, C.; Liang, X.; Jin, H. L.; Niu, S. W. et al. Cooperative Ni(Co)-Ru-P sites activate dehydrogenation for hydrazine oxidation assisting self-powered H₂ production. *Angew. Chem., Int. Ed.* **2023**, *62*, e202308800.

[13] Tang, H. T.; Zhou, H. Y.; Pan, Y. M.; Zhang, J. L.; Cui, F. H.; Li, W. H.; Wang, D. S. Single-atom manganese-catalyzed oxygen evolution drives the electrochemical oxidation of silane to silanol. *Angew. Chem., Int. Ed.* **2024**, *63*, e202315032.

[14] Zheng, X. B.; Yang, J. R.; Li, P.; Jiang, Z. L.; Zhu, P.; Wang, Q. S.; Wu, J. B.; Zhang, E. H.; Sun, W. P.; Dou, S. X. et al. Dual-atom support boosts nickel-catalyzed urea electrooxidation. *Angew. Chem., Int. Ed.* **2023**, *62*, e202217449.

[15] Han, X. B.; Li, Y. G.; Zhang, Z. M.; Tan, H. Q.; Lu, Y.; Wang, E. B. Polyoxometalate-based nickel clusters as visible light-driven water oxidation catalysts. *J. Am. Chem. Soc.* **2015**, *137*, 5486–5493.

[16] Nisar, A.; Zhuang, J.; Wang, X. Construction of amphiphilic polyoxometalate mesostructures as a highly efficient desulfurization catalyst. *Adv. Mater.* **2011**, *23*, 1130–1135.

[17] Xu, X. X.; Gao, X.; Lu, T. T.; Liu, X. X.; Wang, X. L. Hybrid material based on a coordination-complex-modified polyoxometalate nanorod (CC/POMNR) and PPy: A new visible light activated and highly efficient photocatalyst. *J. Mater. Chem. A* **2015**, *3*, 198–206.

[18] Klein, M.; Waldvogel, S. R. Counter electrode reactions-important stumbling blocks on the way to a working electro-organic synthesis. *Angew. Chem., Int. Ed.* **2022**, *61*, e202204140.

[19] Ni, B.; Shi, Y. A.; Wang, X. The sub-nanometer scale as a new focus in nanoscience. *Adv. Mater.* **2018**, *30*, 1802031.

[20] Li, N.; Liu, J.; Dong, B. X.; Lan, Y. Q. Polyoxometalate-based compounds for photo- and electrocatalytic applications. *Angew. Chem., Int. Ed.* **2020**, *59*, 20779–20793.

[21] Miao, J.; Lang, Z. L.; Zhang, X. Y.; Kong, W. G.; Peng, O. W.; Yang, Y.; Wang, S. P.; Cheng, J. J.; He, T. C.; Amini, A. et al. Polyoxometalate-derived hexagonal molybdenum nitrides (MXenes) supported by boron, nitrogen codoped carbon nanotubes for efficient electrochemical hydrogen evolution from seawater. *Adv. Funct. Mater.* **2019**, *29*, 1805893.

[22] Miras, H. N.; Yan, J.; Long, D. L.; Cronin, L. Engineering polyoxometalates with emergent properties. *Chem. Soc. Rev.* **2012**, *41*, 7403–7430.

[23] Miras, H. N.; Vilà-Nadal, L.; Cronin, L. Polyoxometalate based open-frameworks (POM-OFs). *Chem. Soc. Rev.* **2014**, *43*, 5679–5699.

[24] Wang, J.; Lin, C. G.; Li, J. T.; Wei, J.; Song, Y. F.; Guo, J. B. Stabilization and electro-optical switching of liquid crystal blue phases using unpolymerized and polymerized polyoxometalate-based nanoparticles. *Mol. Cryst. Liq. Cryst.* **2016**, *634*, 12–23.

[25] Sun, H.; Xu, X. M.; Jing, C. J.; Shang, W. H.; Wang, Y. C.; Zeng, M. L.; Jia, Z. Y. Composite clusters: $Co_{5.7}Ni_{2.3}W_{12}O_{42}(OH)_4$@fluoro-graphdiyne as a stable electrode for sustained electrochemical oxygen evolution under high current conditions. *Mater. Chem. Front.* **2021**, *5*, 7666–7674.

[26] Yu, B.; Zhang, S. M.; Wang, X. Helical microporous nanorods assembled by polyoxometalate clusters for the photocatalytic oxidation of toluene. *Angew. Chem., Int. Ed.* **2021**, *60*, 17404–17409.

[27] Gultom, N. S.; Abdullah, H.; Hsu, C. N.; Kuo, D. H. Activating nickel iron layer double hydroxide for alkaline hydrogen evolution reaction and overall water splitting by electrodepositing nickel hydroxide. *Chem. Eng. J.* **2021**, *419*, 129608.

[28] Zhou, Y. F.; Wang, Z. X.; Pan, Z. Y.; Liu, L.; Xi, J. Y.; Luo, X. L.; Shen, Y. Exceptional performance of hierarchical Ni-Fe (hydr)oxide@NiCu electrocatalysts for water splitting. *Adv. Mater.* **2019**, *31*, 1806769.

[29] Ji, P. X.; Zheng, D. Y.; Jin, H. H.; Chen, D.; Luo, X.; Yang, J. L.; Wang, Z. B.; Mu, S. C. Ultra-fast *in situ* reconstructed nickel (oxy)hydroxide nanoparticle crosslinked structure for super-efficient alkaline water electrolysis by sacrificing template strategy. *Small Struct.* **2023**, *4*, 2300013.

[30] Shang, W. H.; Wang, Y. C.; Jiang, Y. L.; Wu, M.; Zeng, M. L.; Wang, P.; Qiu, L. L.; Jia, Z. Y. Nanocomposite: Co₄-substituted polyoxometalate@β-FeOOH as high-performance electrocatalysts for oxygen evolution reaction in alkaline conditions. *Appl. Catal. A Gen.* **2022**, *644*, 118810.

[31] Zheng, Y.; Xu, X. X. Surface atom regulation on polyoxometalate electrocatalyst for simultaneous low-voltage H₂ production and phenol degradation. *ACS Appl. Mater. Interfaces* **2020**, *12*, 53739–53748.

[32] Yu, L.; Liang, Q. A fully noble-metal-free electrocatalyst based on a cobalt-polyoxometalate immobilized in a layered double hydroxide for water oxidation at neutral pH. *New J. Chem.* **2022**, *46*, 3073–3077.

[33] Ho, W. H.; Chen, T. Y.; Otake, K. I.; Chen, Y. C.; Wang, Y. S.; Li, J. H.; Chen, H. Y.; Kung, C. W. Polyoxometalate adsorbed in a metal-organic framework for electrocatalytic dopamine oxidation. *Chem. Commun.* **2020**, *56*, 11763–11766.

[34] Yin, D.; Wang, M. L.; Cao, Y. D.; Yang, X. P.; Ji, S. Y.; Hao, H. P.; Gao, G. G.; Fan, L. L.; Liu, H. Polyoxometalate@ZIF induced CoWO₄/WS₂@C-N nanoflower as a highly efficient catalyst for Zn-air batteries. *ACS Appl. Energy Mater.* **2021**, *4*, 6892–6902.

[35] Kozhevnikov, I. V.; Sinnema, A.; Jansen, R. J. J.; van Bekkum, H. ¹⁷O NMR determination of proton sites in solid heteropoly acid $H_3PW_{12}O_{40}$.³¹P, ²⁹Si and ¹⁷ONMR, FT-IR and XRD study of $H_3PW_{12}O_{40}$ and $H_4SiW_{12}O_{40}$ supported on carbon. *Catal. Lett.* **1994**, *27*, 187–197.

[36] Zhao, Z.; Zhang, S. B.; Jin, M.; Zhang, H. M. Pt nanoparticle dispersed Ni(OH)₂ nanosheets via a pulsed laser deposition method efficiently enhanced hydrogen evolution reaction performance in alkaline conditions. *RSC Adv.* **2023**, *13*, 13840–13844.

[37] Lee, S. Y.; Oh, H. J.; Kim, M.; Cho, H. S.; Lee, Y. K. Insights into enhanced activity and durability of hierarchical Fe-doped Ni(OH)₂/Ni catalysts for alkaline oxygen evolution reaction: *In situ* XANES studies. *Appl. Catal. B Environ.* **2023**, *324*, 122269.

[38] Thilagavathi, T.; Venugopal, D.; Thangaraju, D.; Marnadu, R.; Palanivel, B.; Imran, M.; Shkir, M.; Ubaidullah, M.; AlFaify, S. A facile co-precipitation synthesis of novel WO₃/NiWO₄ nanocomposite with improved photocatalytic activity. *Mater. Sci. Semicond. Process.* **2021**, *133*, 105970.

[39] Wang, J.; Ciucci, F. *In-situ* synthesis of bimetallic phosphide with carbon tubes as an active electrocatalyst for oxygen evolution reaction. *Appl. Catal B Environ.* **2019**, *254*, 292–299.